Front. Struct. Civ. Eng.
https://doi.org/10.1007/s11709-020-0615-6

RESEARCH ARTICLE

Seismic behavior of cantilever wall embedded in dry and saturated sand

Sanku KONAI, Aniruddha SENGUPTA, Kousik DEB*

Department of Civil Engineering, Indian Institute of Technology Kharagpur, Kharagpur 721302, India
**Corresponding author. E-mail: kousik@civil.iitkgp.ac.in*

ABSTRACT The embedded cantilever retaining walls are often required for excavation to construct the underground facilities. Significant numbers of numerical and experimental studies have been performed to understand the behavior of embedded cantilever retaining walls under static condition. However, very limited studies have been conducted on the behavior of embedded retaining walls under seismic condition. In this paper, the behavior of a small scale model embedded cantilever retaining wall in dry and saturated sand under seismic loading condition is investigated by shake table tests in the laboratory and numerically using software FLAC2D. The embedded cantilever walls are subjected to sinusoidal dynamic motions. The behaviors of the cantilever walls in terms of lateral displacement and bending moment are studied with the variation of the two important design parameters, peak amplitude of the base motions and excavation depth. The variation of the pore water pressures within the sand is also observed in the cases of saturated sand. The maximum lateral displacement of a cantilever wall due to seismic loading is below 1% of the total height of the wall in dry sand, but in case of saturated sand, it can go up to 12.75% of the total height of the wall.

KEYWORDS embedded cantilever wall, shake table test, FLAC2D, seismic loading, saturated and dry sand

1 Introduction

Embedded cantilever retaining walls are frequently used for carrying out excavation work to install utility pipelines or to construct building foundations in an urban setting. A cantilever wall embedded in a soil is a sand-structure interaction problem and the behavior of such a wall during seismic conditions is not fully understood. The horizontal displacement of a retaining wall induces settlement at the adjacent ground surfaces [1,2] and it may cause damages to the nearby structures. Various researches are conducted to study the damage of such brittle material by various researchers [3–7]. The failure of sand under seismic loading can also be investigated by applying a recently popular method called phase field method [8–12].

The dynamic responses of an embedded wall depend on the properties of the adjacent sands, properties of the wall, nature of the ground motions, etc. One of the popular methods to obtain earth pressures behind a retaining structure under seismic condition is Mononobe-Okabe method [13,14]. This method is a pseudo-static method based on Coulomb's wedge theory. The design of retaining structures based on pseudo-dynamic analysis [15] and the displacement based sliding block method [16] are also used for the seismic design of retaining walls. A performance based design of a flexible cantilever retaining wall is proposed by Callisto and Soccodato [17]. It is found that the seismic performance of an embedded cantilever retaining wall is mostly related to the strength of the sand-wall system. Conti et al. [18] performed centrifuge tests on small scale models on a pair of retaining walls in dry sand. It is seen that for maximum accelerations, which are smaller than the critical limit equilibrium value, the retaining walls experience a significant permanent deformation under increasing structural loads. For larger accelerations, the walls rotate under constant internal forces. It is also observed that no significant deformation is measured, if the present earthquake motion is less severe than the earthquakes motions previously experienced by the wall. Khosrojerdi and Pak [19] performed a numerical analysis using finite element program (PISA) on the seismic response of a gravity waterfront structures. It is

Article history: Received Mar 5, 2019; Accepted May 30, 2019

found that the pore pressure generation is more in loose sand than in dense sand. Numerical investigations have also showed that increasing 20% relative density of a sand can lead to 15% reduction in horizontal displacement of a quay wall. Tricarico et al. [20] carried out experimental analysis under sinusoidal dynamic loadings by centrifuge model tests on cantilever and propped retaining wall considering saturated sand. Their results have shown that as far as amplification of wave is concerned, there is a significant difference in sand structure system in dry sand as against in saturated sand. It is found that liquefaction of sand occurred in case of loose sand and accumulated displacement is higher in saturated sand due to the generation of pore water pressures in the sand. Studies are conducted on seismic behavior of strutted or braced structures considering sand-structure interaction [21,22].

Apart from these studies there are many significant studies [23–32] on a retaining structure or wall under seismic condition, which have shown the vulnerability of these types of structure during earthquake. The presence of water in the sand where these types of structures are located increases the vulnerability of these structures. The reason behind this is the generation excess pore water pressures in the sand due to the dynamic forces. The excess pore pressures reduce the effective stresses in the sand as well as the strength of the sand. Although a number of studies, as discussed above, have been conducted in the past but still the behaviors of an embedded cantilever wall under seismic loading are yet to be fully understood. This paper presents a series of numerical and experimental analyses on a small scale model of a pair of cantilever retaining walls embedded in a sand to understand its performances under different seismic loadings. A two dimensional numerical model is developed by using a commercial software, FLAC2D. In this numerical study, a pair of cantilever walls embedded in a dry and a saturated sand is subjected to sinusoidal seismic accelerations. The responses of the walls under different peak amplitudes of base motions and excavation depths are studied.

2 Experimental setup

A small scale physical model of a pair of cantilever walls, made of plexiglass material and embedded fully in local sand, is tested in the laboratory on a shake table. The experimental setup (refer to Figs. 1 and 2) consists of a shake table which essentially comprises of a 1 m × 1 m steel table mounted on rails. The table is attached to an actuator which vibrates the table in a uniaxial horizontal direction. The servo hydraulic actuator has a capacity of +/– 50 kN. It has a stroke length of +/–100 mm. The actuator is driven by a controller which has a capability of accepting an actual earthquake (random, cyclic) loading as input and generating it between 0.01 and 50 Hz frequencies. The actuator has the capability to hold and restart the loading during a test. It also allows one to increase the base motion's frequency and amplitude during a test. The tests are performed in a rigid plexiglass tank, fixed to the shake table, with inside dimensions of 885 mm (length) × 800 mm (width) × 400 mm (height). The edges of the 16 mm thick plexiglass test tank are reinforced with steel angles. A thick layer of absorbing pad is placed on the three inner sides of the tank to reduce reflection/refraction of waves at the ends in the model test [33]. Each of the model cantilever walls are 200 mm in height, 2.4 mm in thickness, and 885 mm in length and made of plaxiglass material with density and modulus of elasticity of 1010 kg/m^3 and 6.3 × 10^9 Pa, respectively. The small scale test is designed according to the 1-g scaling law proposed by Meymand [34]. The test chamber is initially filled up to a depth of 200 mm with dry sand in two lifts of 100 mm each, maintaining a uniform density of 1600 kg/m^3 (unit weight = 15.7 kN/m^3). The paired walls with the removable support system at the top to maintain a gap (B) of 160 mm between the two walls are then placed over the sand bed in the middle of the test tank and the sand filling is continued as before. The sand filling and the subsequent compaction is done in four layers with the thickness of each layer being 100 mm. In case of the model tests in

Table 1 List of laboratory shake table tests on dry and saturated sand

sand condition	test	D_e (mm)	D_b (mm)	D_e/H	t_w (mm)	Z (mm)	B (mm)	maximum amplitude of the base acceleration
dry sand	CW1	80	120	0.4	2.4	400	160	0.1g
	CW2	80	120	0.4	2.4	400	160	0.15g
	CW3	80	120	0.4	2.4	400	160	0.2g
	CW4	60	140	0.3	2.4	400	160	0.1g
	CW5	100	100	0.5	2.4	400	160	0.1g
saturated sand	CWU1	80	120	0.4	2.4	400	160	0.1g
	CWU2	80	120	0.4	2.4	400	160	0.15g
	CWU3	80	120	0.4	2.4	400	160	0.2g
	CWU4	60	140	0.3	2.4	400	160	0.1g
	CWU5	100	100	0.5	2.4	400	160	0.1g

Note: CW = cantilever wall, CWU = cantilever wall in undrained condition.

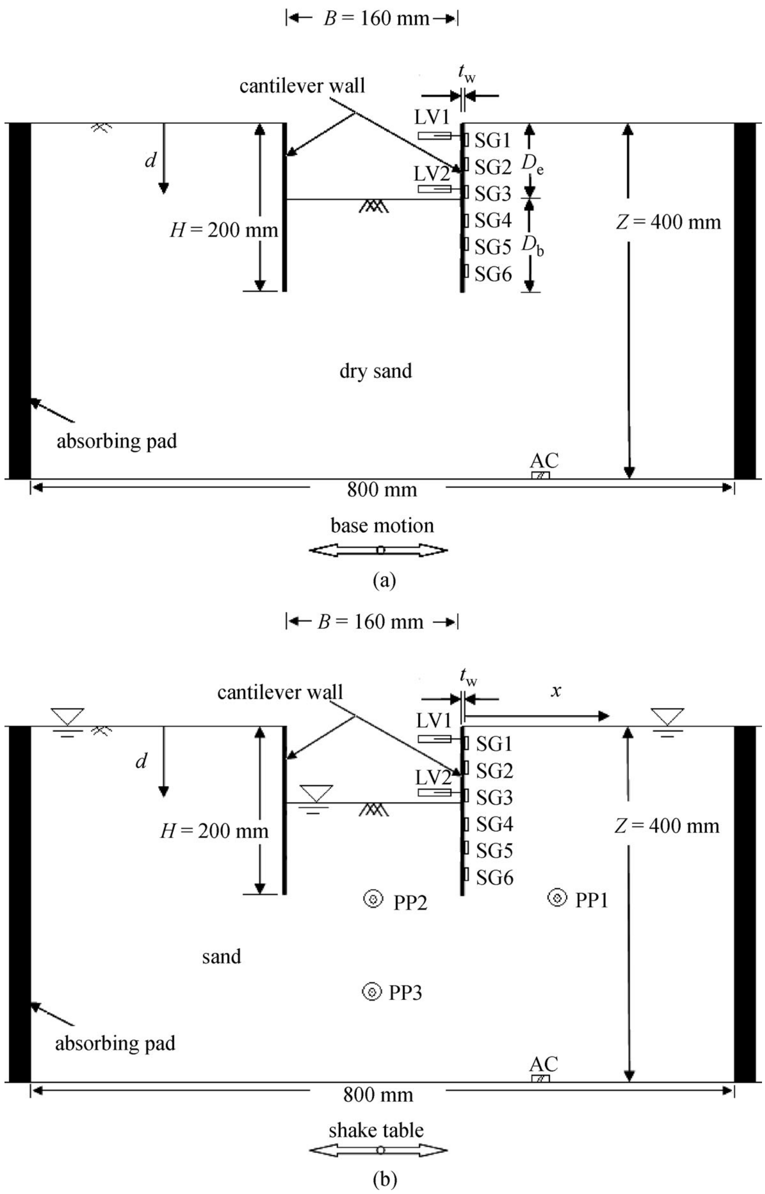

Fig. 1 Schematic diagram of laboratory test set up for the embedded cantilever walls in (a) dry sand and (b) saturated sand under dynamic loading condition.

saturated sand, after the compaction and the filling with dry sand are complete, the required amount of water is added for complete saturation of the sand. The density and the water content of the sand are maintained almost uniform with the depth. In all the experiments under saturated condition, the water table is maintained at the top of the sand surface. Once the filling and the compaction processes are over, the support system at the top of the walls are removed. Next, the sand between the two embedded cantilever walls is excavated up to a depth of 80 mm (CWU1 test) from the top. Then, in cases of the tests with water table maintained at the top, the water within the excavation between the two walls is dewatered to maintain the water table within the excavation at the excavation level (D_e). The responses of the right cantilever wall are only considered in this study. Six numbers of strain gauges (SG1-6) are attached to the right cantilever retaining wall at different depths. Two numbers of linearly variable differential transformers (LVDTs) are also attached at different heights of the wall to directly measure the displacements at those locations as shown in Fig. 1. The LVDTs used in the experiments have a least count of 0.01 mm and have maximum measuring capacity of 20 mm. The lateral displacements of the retaining wall after a dynamic event are calculated from the LVDT measurements (these are also used as boundary conditions during the integration to obtain displacement.) and by double integrating the obtained equation of the curvature

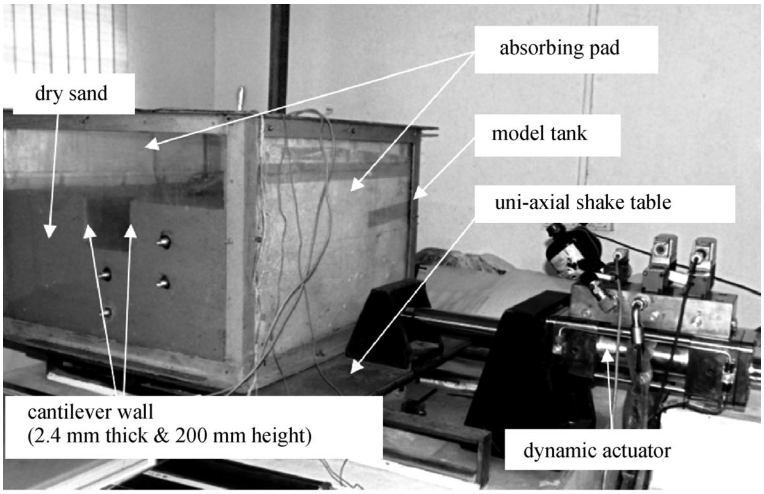

(a)

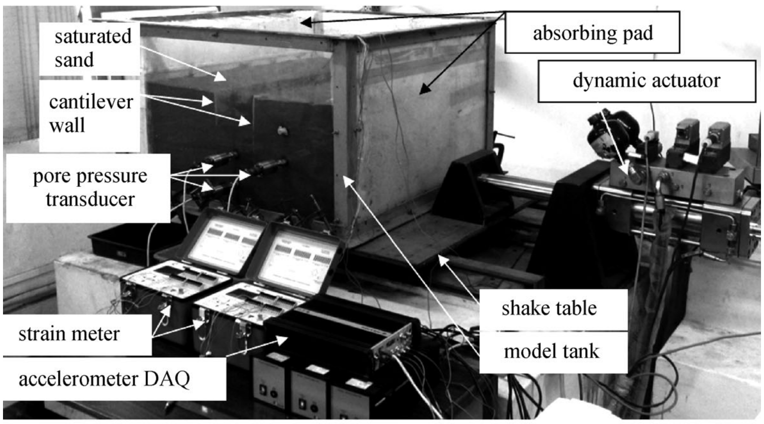

(b)

Fig. 2 Laboratory model test setup with cantilever walls embedded in (a) dry sand (b) saturated sand.

with length of the deflected wall (obtained from the strain gauge readings). The bending moments in the retaining wall are back calculated from the strain gauge readings. An accelerometer (AC) is attached at the bottom of the sand layer to measure the motions at the bottom of the sand layer, as shown in Fig. 1. In case of tests with saturated sand, three numbers of pore pressure transducers (PP1, PP2, and PP3) with per second data recording capabilities are placed at different depths in the sand for measuring the pore water pressures generated in the sand during a shake table test. No pore pressure transducers are used for tests in dry sand. In the reference test, CWU1 (refer to Table 1), PP1 is placed at 200 mm (1*H*) from the top sand surface and 100 mm (0.5*H*) away from right wall (Fig. 1). The pore pressure transducers, PP2 and PP3 are placed 120 mm (0.6*H*) and 220 mm (1.1*H*) below the excavation level, respectively, and in the middle of the excavation width (*B*), as shown in Fig. 1. Sinusoidal motions of specified amplitude, frequency and number of cycles are applied to the test tank so that the effect of these parameters on the walls may be studied. In the present paper, the performance of the cantilever embedded walls are presented for a 4 s of sinusoidal motions at different peak amplitudes and at a constant frequency of 2 Hz. Figures 3(a), 3(b), and 3(c) show the sinusoidal motions applied to the shake table with the peak amplitude of 0.1*g*, 0.15*g*, and 0.2*g*, respectively. The used sinusoidal motion is a dynamic loading. However, it can be used to represent a seismic load and has been used to study the effect amplitude of a motion. An earthquake motion contains a large number of frequencies and it is not convenient for the parametric study. Seed and Idriss [35] have given a procedure to convert an actual earthquake motion into equivalent cycles of sinusoidal motions with constant amplitude and frequency, which has been also used by Banerjee et al. [36].

3 Sand properties

The sand utilized in all the shake table tests is obtained locally from Kasai River and is henceforth referred to as Kasai River sand. The grain size distribution of the sand is

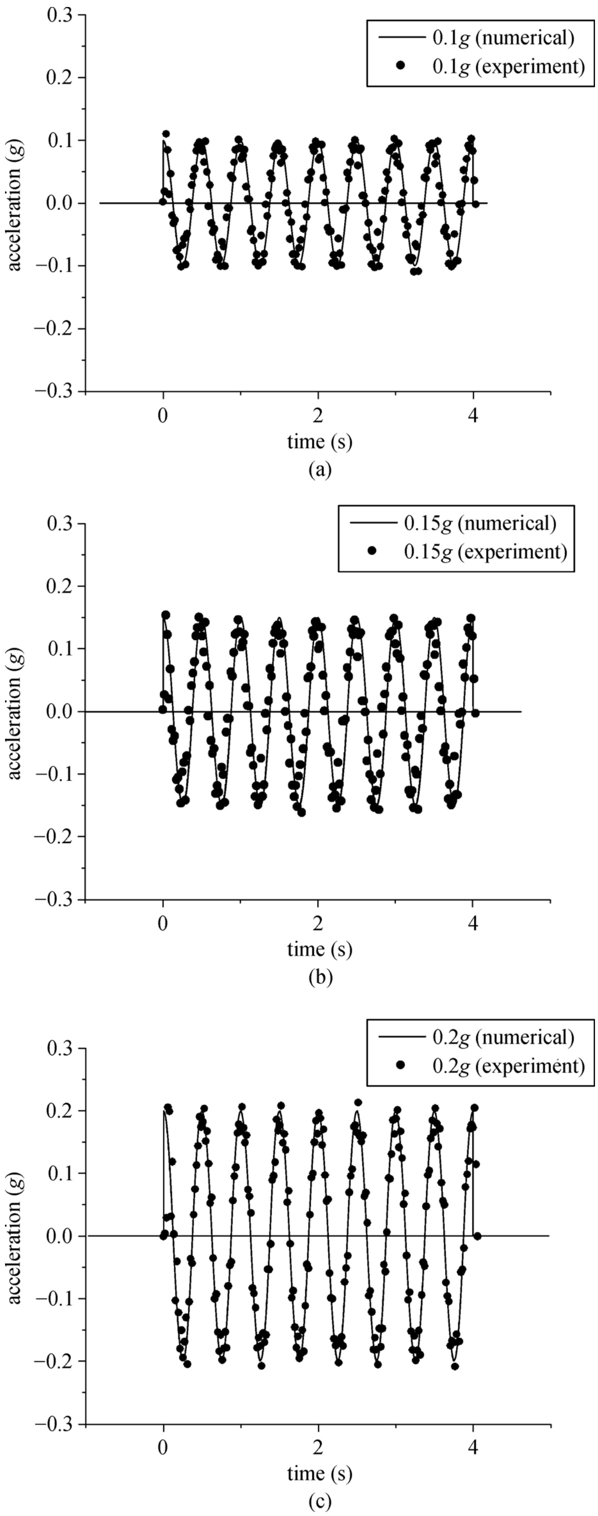

Fig. 3 Sinusoidal motions applied at the bottom of the sand in the laboratory experiments and numerical analyses with peak amplitude of (a) 0.1g, (b) 0.15g, and (c) 0.2g.

shown in Fig. 4. It is classified as poorly graded sand (SP), according to the Unified Soil Classification System (USCS). The specific gravity of the sand is 2.67. The maximum dry unit weight $\gamma_{d(max)}$ is 16.7 kN/m^3 and the minimum dry unit weight $\gamma_{d(min)}$ is 14.13 kN/m^3. The uniformity coefficient and coefficient of curvature of the sand are found to be 2.84 and 0.87, respectively. Tsuchida [37] proposed the boundaries of potentially liquefiable sand and most liquefiable sand which are also shown in Fig. 4. It may be seen from the figure that the Kasai River sand is within the range of most liquefiable sand. In all the model tests, the bulk unit weight of the sand is maintained as 15.7 kN/m^3 (at a relative density of 65%). The drained triaxial shear tests are performed on the sand samples to find its shear strength parameters. The effective angle of friction (ϕ') of the sand for this study is 38°. The coefficient of lateral earth pressure for the sand is 0.38 as calculated by the well known formula [$K_h = (1-\sin\phi')$].

4 Numerical modeling

The behaviors of the small scale plexiglass cantilever walls embedded in sand under dynamic conditions, as tested on the shake table, are also analyzed by a two dimensional, plane strain, finite difference commercial software called FLAC 2D [38]. The liquefaction problem itself is quite complicated to model. In a braced excavation the length to width ratio is very large and as such it can be properly represented as a 2-D plane-strain problem without any significant error. A 3-D analysis is time consuming and may not be worth pursuing. Similar 2-D studies are also conducted by various researchers for similar type braced excavation problems [17,21,39–42].

Each of the 200 mm high and 2.4 mm wide model cantilever walls is discretized by 10 two-dimensional beam elements. The published properties of a plexiglass material are adopted to model the cantilever walls. For the present plane strain analyses, the Young's modulus of the walls are calculated using $E_{pp} = E_p/(1-\mu_p^2)$ [38] where the Young's Modulus of plexiglass (E_p) and the Poisson ratio (μ_p) are taken as 6.3×10^9 N/m^2 and 0.35, respectively. A mesh size of 20 mm × 20 mm is adopted for the walls. The 800 mm × 400 mm foundation sand within which the cantilever walls are embedded is discretized by 760 rectangular 4-noded grids. Figure 5 shows the numerical discretization of the whole system. The actual construction sequences of the walls are not modeled. The seismic analysis is performed after the completion of final stage of excavation between the walls and the responses of the cantilever walls are reported for the seismic loading conditions only.

Three different depths of excavation (D_e), 60, 80, and 100 mm, between the embedded cantilever walls have been considered here as in the laboratory model tests as well as in the numerical analyses. In case of saturated sand, as in the laboratory experiments, the water table is kept at ground surface outside the excavation and it is lowered to excavation level within the excavation. In the numerical analysis, the bottom boundary is considered to be fixed,

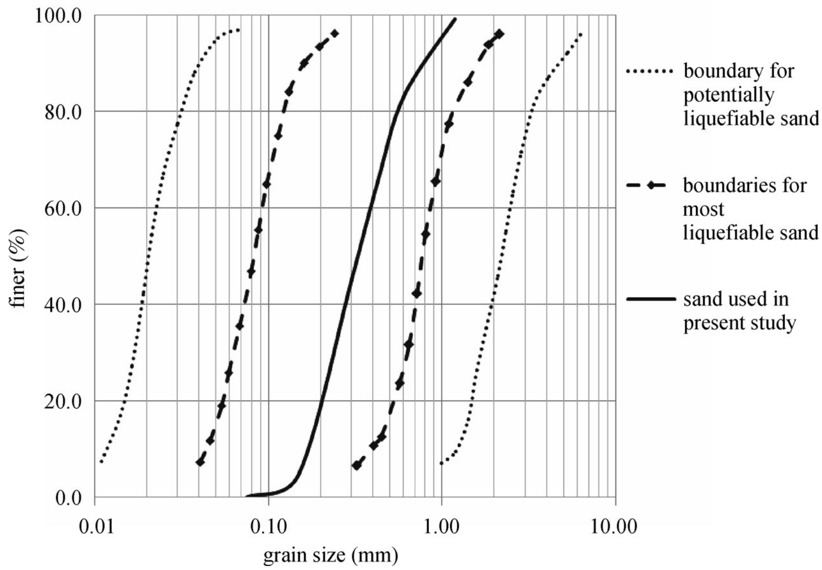

Fig. 4 Grain size distribution of Kasai River sand used in the present study and the boundaries of the liquefaction susceptible sand.

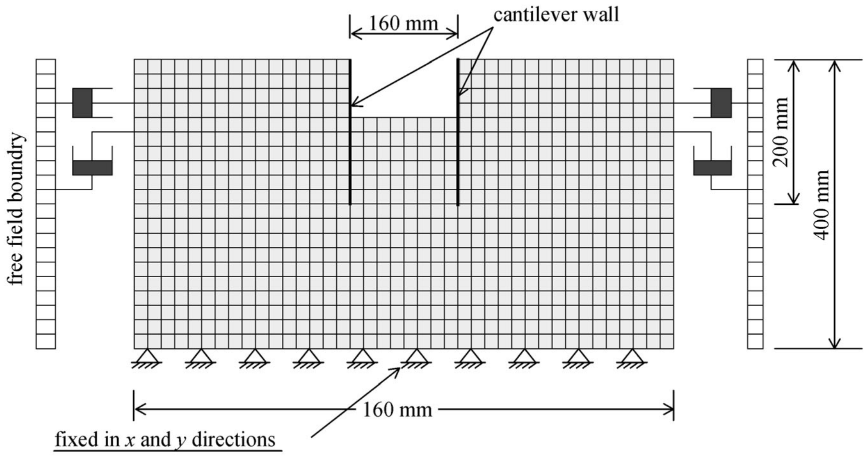

Fig. 5 Numerical discretization of the cantilever walls embedded in sand.

that is, the movements in both x and y directions are restricted. The nodes on the two extreme side boundaries are on roller, that is, the movements in the horizontal direction are restricted. In the dynamic analyses, the free field conditions are applied to the two vertical side boundaries in order to minimize the reflection/refraction of waves at these boundaries. Material parameters used in the numerical model are presented in Table 2.

In the numerical analyses, the sand is assumed to be an elastic, perfectly plastic (Mohr-Coulomb) material. The Mohr-Coulomb model has been found to be simple but accurate enough to represent the constitutive behavior of sand under dynamic condition [17,18,21,39–42]. Under dynamic loading, undrained behavior (no volume change, only pore water pressure generation) of sand prevails. Thus, there is no good reason to use advanced sophisticated models which are more applicable to sand with volume change. The elastic modulus of the sand have been

Table 2 Material parameters used for the numerical analyses

sand condition	unit weight of sand (kN/ m^3)	friction angle (ϕ') (degree)	shear modulus (G) of sand (kPa)	Poisson's ratio (μ_s) of sand	stiffness (EI) of cantilever wall ($N \cdot m^2/m$)
dry	15.7	38°	2.1×10^3	0.3	7.29
saturated	19.7	38°	1.66×10^3	0.3	7.29

found from the Janbu [43] expression as

$$E_s = P_{ref} K_d \left[\frac{(\sigma_c)}{P_{ref}} \right]^n, \tag{1}$$

where P_{ref} = 100 kPa, σ_c = confining pressure. The values of K_d and n are obtained from the laboratory drained triaxial tests on the sand and are 402 and 0.5, respectively, for the Kasai River sand. To model the dynamic (mechanical) behavior of Kasai River sand, a modulus degradation curve is suggested. The resonant column (for low strain) tests and the cyclic triaxial tests (for high strain) data for Kasai River sand given by Chattaraj and Sengupta [44] at 100 kPa confining pressure are considered in the present study. A curve is fitted through the test data for 100 kPa using Eq. (2a) developed by Hardin and Drnevich [45] with constant a = 1.3 and b = 1.0 (refer to Aggour and Zhang [46]). The modulus reduction curve has been scaled for the average confining pressure existing in the small scale model using Eq. (2b).

$$M_e = G/G_{max} = 1/[1 + a(\gamma_e/\gamma_r)^b], \tag{2a}$$

where γ_e is the cyclic shear strain and γ_r is reference shear strain of the sand. Considering the combined effects of plasticity index and different confining pressures, Ishibashi and Zhang [47] have proposed Eq. (2b) for the modulus reduction curve of a general sand (refer to Kramer [48]). *PI* value is taken as zero and an average confining pressure is considered for the present study to obtain the modulus reduction curve for the present sand from Eq. (2b).

$$M_e = G/G_{max} = K(\gamma_e, PI)(\sigma'_m)^{m(\gamma_e, PI) - m_0}, \tag{2b}$$

where

$$K(\gamma_e, PI) = 0.5 \left\{ 1 + \tanh \left[\ln \left(\frac{0.000102 + n(PI)}{\gamma_e} \right)^{0.492} \right] \right\},$$

and

$$m(\gamma_e, PI) - m_0 = 0.272 \left\{ 1 - \tanh \left[\ln \left(\frac{0.000556}{\gamma_e} \right)^{0.4} \right] \right\}$$

$$\exp(-0.0145 PI^{1.3}),$$

when $PI = 0$ then, $n(PI) = 0$, where PI is the plasticity index of the sand and σ'_m is the effective mean confining pressure. Figure 6 shows the curves obtained for 100 kPa confining pressure developed from Chattaraj and Sengupta [44] and Hardin and Drnevich [45]. Figure 6 also shows the curves for average confining pressure of the present study obtained from Hardin and Drnevich [45] and Ishibashi and Zhang [47].

The "Sigmoidal (sig4)" model available in FLAC2D [38] expresses the degradation of the modulus of a sand with the shear strains by Eq. (2c). The model simulation in FLAC2D using the "Sigmoidal" model for present confining pressure is shown in Eq. (6).

$$M_e = y_0 + \frac{a'}{1 + \exp[-(L - x_0)/b']}, \tag{2c}$$

where L is the logarithmic strain and given by $L = \log_{10}(\gamma_e)$, where γ_e is the cyclic shear strain in the sand. The parameters a', b', x_0, and y_0 are the curve fitting parameters whose values are 0.96, –0.4, –2.0, and –0.03, respectively, corresponding to the best fit curve shown in Fig. 6. The sand behavior under cyclic loading can be represented by the relationship between M_e and γ_e [38]. Under plane strain condition, the shear stress (τ), and the shear strain (γ_e) can be related as:

$$\frac{\tau}{G_0} = \frac{G_s(\gamma_e)}{G_0}\gamma_e = M_e(\gamma_e) \cdot \gamma_e, \tag{3}$$

where $G_s(\gamma_e)$ is the secant shear modulus which is a function of γ_e. G_0 is the small strain shear modulus and M_e is the normalized secant shear modulus.

In the present model, the test box is not considered. A very thin gap is maintained between the test box and the plexiglass cantilever walls to avoid any interaction between them at the edges. However, the sand-structure interaction between the foundation sand and the walls is modeled by using a shear and a normal spring at each node of the structures. The normal and shear stiffness (K_n and K_s) are estimated [38] as:

$$K_n = K_s = 10 \max \left[\frac{\left(K + \frac{4}{3} G \right)}{\Delta z_{min}} \right], \tag{4}$$

where K is the bulk modulus of the sand, G is the shear modulus of the sand, and Δz_{min} is the smallest width of the adjoining zone in the normal direction to the interface. The interface friction angle between the plexiglass walls and the sand is estimated to be 20°. The coefficient of lateral earth pressure for the sand is taken be 0.38 for the sand as mentioned earlier.

In the numerical analysis, the 'Finn model' model is used to generate the excess pore water pressures for the dynamic conditions in case of saturated sand. Martin et al. [49] proposed 'Finn model' and later this model is modified by Byrne et al. [50]. In the 'Finn model', the change in the pore water pressure is given by

$$\Delta u = M_s \Delta \varepsilon^p, \tag{5}$$

where Δu is the change in the pore water pressure, M_s is the constrained modulus of the sand. $\Delta\varepsilon^p$ is the change in volumetric strain and is given by $\gamma_s C_1 \exp(-C_2 \varepsilon_{vd}/\gamma_s)$, where, ε_{vd} is the change in the volumetric strain, C_1 is a constant and given as $7600(D_r)^{-2.5}$, C_2 is another constant and given by $0.4/C_1$, D_r is the relative density of the sand and γ_s is the shear strain in the sand. As mentioned earlier, the relative density (D_r) is maintained at 65% in the tests. The values of C_1, C_2 used in this analysis are 0.2231 and 1.79, respectively.

In the numerical analyses, a parametric study on the effect of the peak amplitude of the base motions and the excavation depth (D_e) are performed. The numerical results are compared with the corresponding experimental results for both dry and saturated sand conditions. The performances of the embedded cantilever walls in terms of the lateral displacements (u) of the wall, the bending moments (M) in the wall and the ground surface settlements (v) in the vicinity are obtained from these analyses.

5 Results and discussions

All the laboratory model shake table tests mentioned in Table 1 are conducted with identical sand in dry and saturated conditions. Similarly, numerical analyses for all the cases mentioned in Table 1 are also performed for the same conditions. The obtained results from these studies that are for the dynamic loading conditions only and they are presented in non-dimensional forms for the convenience. The lateral displacement (u) of the right hand embedded cantilever wall obtained from the laboratory model tests and the numerical analyses are normalized with respect to the total depth of wall (H), i.e., u/H. The bending moments (M) in the wall are normalized with respect to $\gamma' H^3$, i.e., $M/\gamma' H^3$, where γ' is the effective unit weight of the sand. The depth from the ground surface, d is normalized with respect to total height of the wall, H. The excavation depth, D_e is also normalized with respect to the total depth of the wall (H). The total height (H) of the cantilever wall and width of the excavation (B) are kept identical for all the cases. It is a well know that in the case of saturated sand, excess pore water pressures (Δu) are generated under dynamic loadings. The reduction of effective stresses in a sand is caused by this generation of excess pore water pressures (Δu) which ultimately weakens the sand strength and may lead to large deformations and failure in the embedded structures. The developed excess pore water pressures (Δu) in the sand divided by the initial vertical effective stress (σ'_{v0}) in the sand is defined as the pore water pressure ratio, r_u. If r_u reaches unity then the sand fully liquefies and the strength of the sand becomes zero. The pore water pressures developed during the shake table tests in saturated sand are measured by PP1, PP2, and PP3, three pore water pressure transducers which are located at three different locations in the sand. As mentioned earlier in CWU1 test (Table 1), the pore pressure transducer PP1 is placed at $1H$ below from the top sand surface and $0.5H$ away from the right cantilever wall. The transducers, PP2 and PP3 are placed at $0.6H$ and $1.1H$ below the excavation level, respectively, where H is total height of the retaining walls. In the numerical analyses, the pore water pressures are also obtained at the same locations for comparison with the experimental results. Figures 7(a), 7(b), and 7(c) show the variations of r_u with time in the CWU1 test. From the results of the corresponding numerical analysis, it may be observed that the maximum value of r_u is 0.6 (refer to Fig. 7(a)) for PP1 which is $0.5H$ away from the wall and

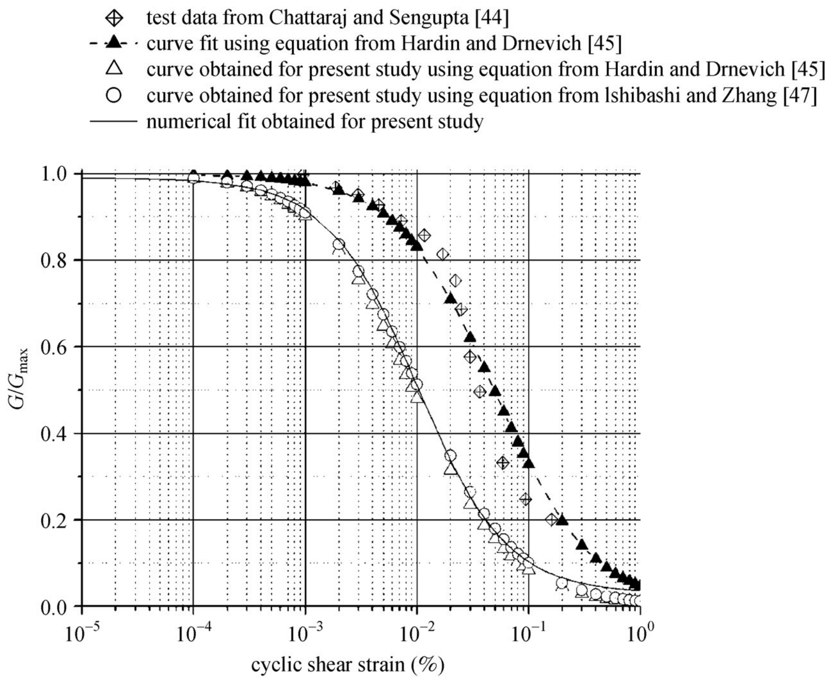

Fig. 6 Modulus of degradation curve for Kasai River sand.

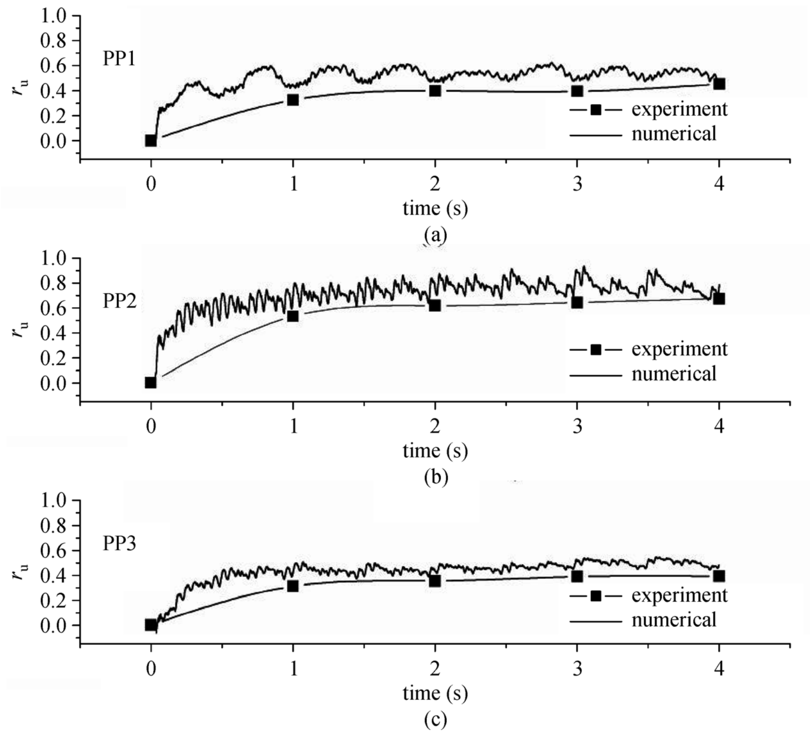

Fig. 7 Variation of pore pressure ratios (r_u) for (a) PP1, (b) PP2, and (c) PP3 with time for CWU1 test.

1H depth below the ground surface. But from Fig. 7(b), it may be seen that this r_u reaches 0.8 for PP2 which is located 0.6H below the excavation level. The development of excess pore water pressures in the sand is more below the excavation level than those in the adjacent to the walls. Higher values for r_u imply lower effective stresses which ultimately causes reduction in the strength of the sand below the excavation level leading to greater damages to the cantilever walls in a saturated sand than in a dry sand. The values obtained from the pore pressure transducers are in reasonably good agreement with the numerical results. Since the data acquisition system for the pore pressure transducers have per second data recording capabilities, the exact variation pore pressure variations with time is not obtained in the laboratory model tests.

Figures 8(a) and 8(b) show the comparison of the normalized lateral displacement (u/H) in dry and saturated sand for 0.1g peak amplitude of base motions. Figure 8(a) shows the responses of the cantilever wall at the end of the dynamic loadings. The numerical results are found to be in reasonable agreement with the experimental results. It may be seen from the figure that the maximum lateral displacement occurs near the ground surface in both dry and saturated sands, but the lateral displacements in case of saturated sand are significantly higher. The variations of the lateral displacements of the wall (u/H) with time are presented in Fig. 8(b) for the dry and the saturated sand. It shows that the maximum lateral displacement occurs at the end of the dynamic loading event. From the numerical and the experimental analyses, it is observed that when the normalized excavation depth (D_e/H) is 0.4 and the peak amplitude of the base motion is 0.1g, the maximum normalized lateral displacement (u/H) is 0.0033 and 0.004, respectively, in dry condition. In the saturated sand, they are 0.0501 and 0.041, respectively. The present of water in the sand causes the huge lateral displacements in embedded cantilever walls under seismic loading due to the reduction in strength or weakening of sand.

The normalized bending moment ($M/\gamma'H^3$) distribution along the cantilever wall over the time are presented in Figs. 9(a) and 9(b) for the walls embedded in the dry and the saturated sand, respectively. From the numerical analyses and the experiments, it is found that that the maximum bending moment (M) occurs below the excavation level in both dry and saturated sand. But there is an increase in the bending moments (M) in the wall in case of wall embedded in the saturated sand. The maximum normalized bending moment ($M/\gamma'H^3$) in the wall is 0.0042 and 0.0036, respectively, in the wall embedded in the dry sand, and 0.091 and 0.0086, respectively, in the wall embedded in the saturated sand. Figure 9(b) shows that the maximum bending moment in the cantilever wall occurs at the end of the cyclic loading for the dry sand. Whereas for the wall embedded in the saturated sand, the maximum bending moment occurs during the shaking. In the experimental and the numerical studies, the peak amplitudes of the base motions and the excavation depth are varied to find their effects on the performance of the

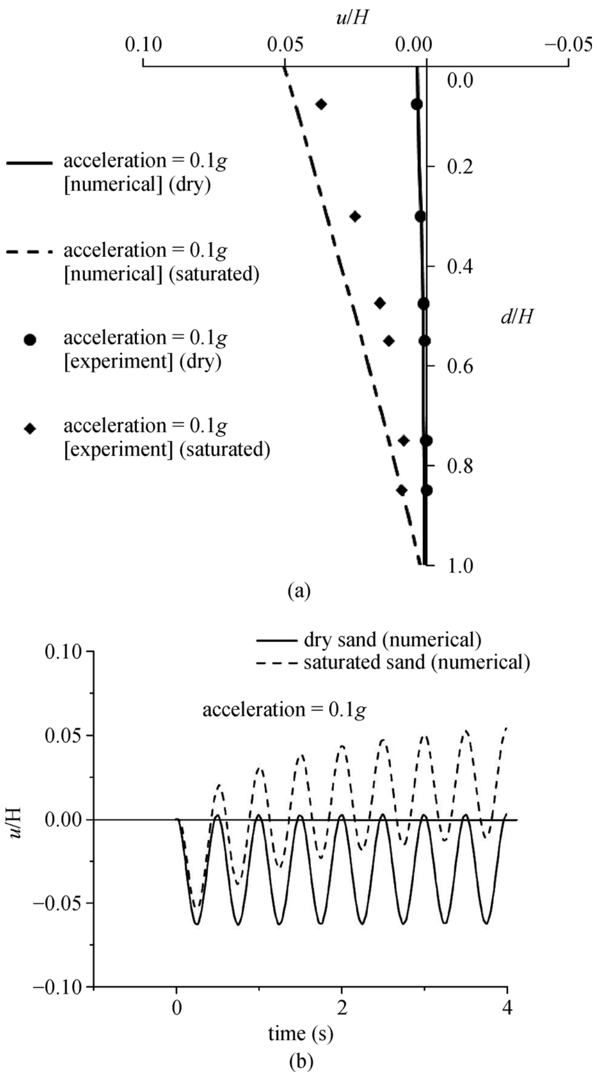

Fig. 8 Comparison of lateral displacements (u/H) of wall: (a) at the end of the cyclic loadings; (b) during cyclic loadings in the dry and the saturated sand.

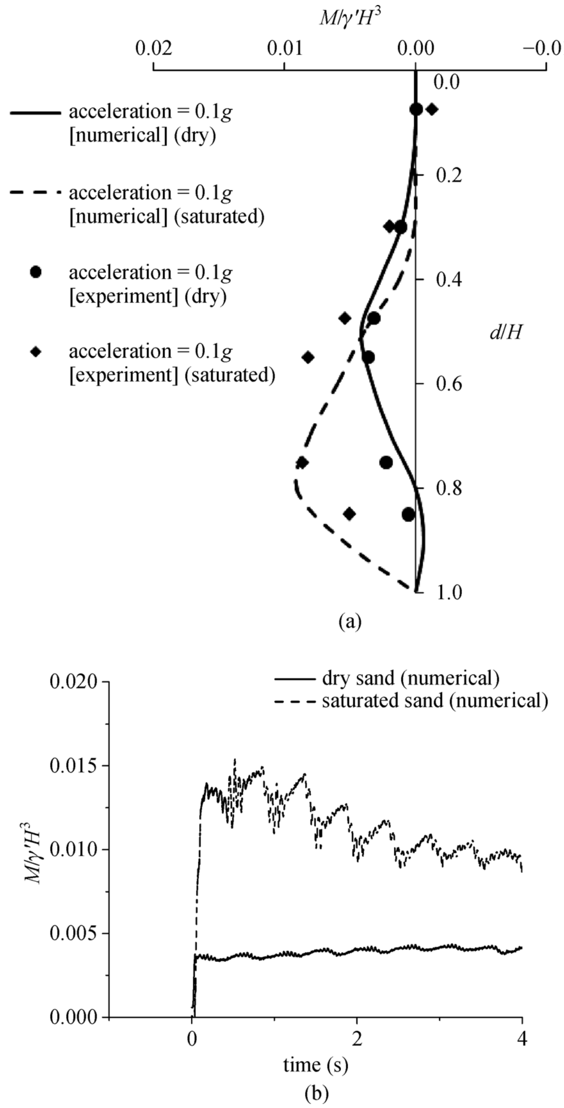

Fig. 9 Comparison of the bending moments ($M/\gamma'H^3$) in the wall: (a) at the end of the cyclic loadings; (b) during the cyclic loadings in the dry and the saturated sand

flexible embedded cantilever wall in the dry and the saturated sand.

5.1 Effect of peak amplitude of base motions

Several tests (CW1, CW2, CW3, CWU1, CWU2, CWU3) are conducted with different peak amplitude of the base motions keeping the excavation depth constant at $D_e = 0.4H$ in both dry and saturated sand. All the other parameters are kept identical for these tests. In this study, the amplitude of 0.1g, 0.15g, and 0.2g are considered for the sinusoidal base motions. These base motions are shown in Figs. 3(a), 3(b) and 3(c). Larger amplitude of motions imparts larger forces on the walls and causes larger damage to the walls in both dry and saturated sand. In case of walls embedded in the saturated sand, due to the increase in the pore pressures and subsequent reduction in the effective stresses in the sand, the lateral displacements of the cantilever walls embedded in saturated sand is much more as compared to those for the walls in dry sand under the same amplitude of base motions. In Fig. 10, it may be seen that the values of pore pressure ratios (r_u) corresponding to PP3 increase with increase in peak amplitude of the base motions. A complete liquefaction of the sand occurs when the pore water pressure ratio (r_u) reaches unity or close to it. In this study, the pore water pressure ratios (r_u) are not reaching unity, therefore a complete liquefaction is not observed. In case of 0.1g base motions, the maximum pore water pressure ratios (r_u) are close to 0.5, which is less that the pore water pressure ratios (r_u) of 0.68 and 0.8 developed during the 0.15g and 0.2g base motions, respectively. The generation of more pore water pressures

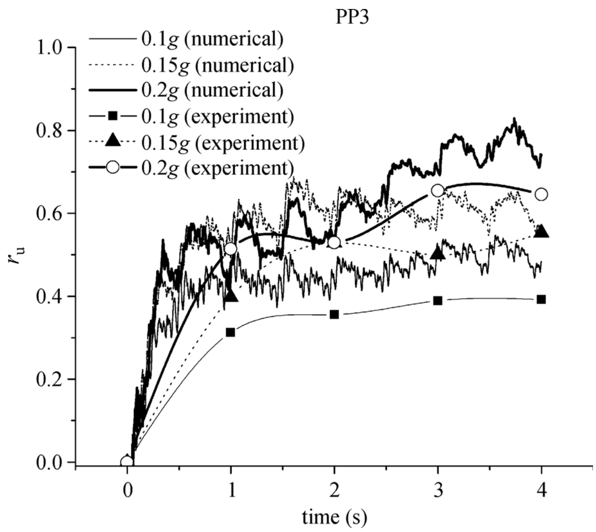

Fig. 10 Variation of pore water pressure ratios (r_u) at PP3 with time for different peak amplitudes of the base motions.

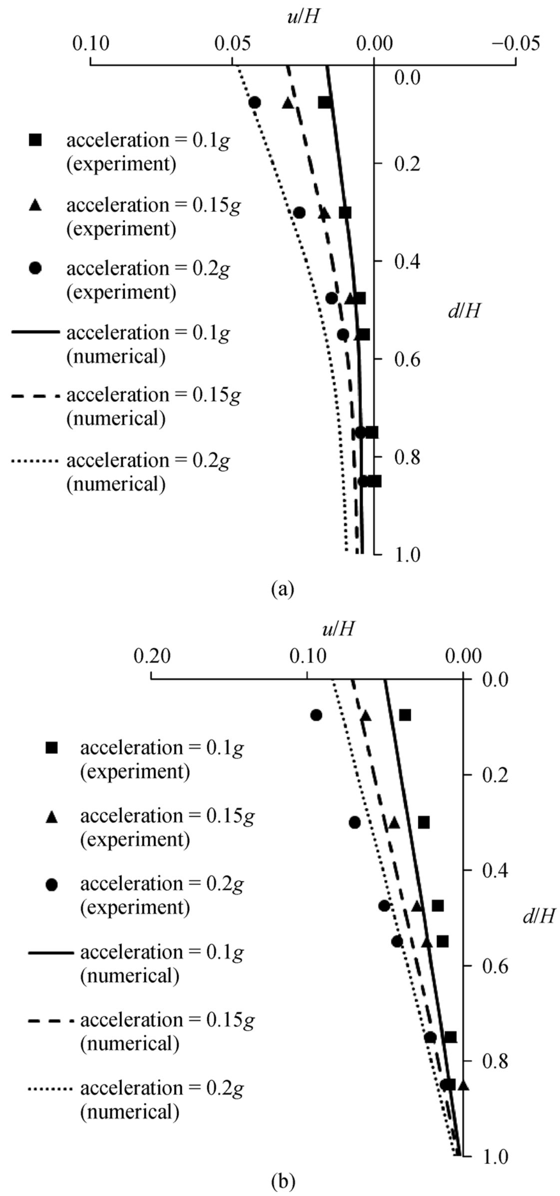

Fig. 11 Lateral displacements of the embedded cantilever wall under different peak amplitudes of the base motions in (a) dry sand and (b) saturated sand.

in the sand for higher amplitudes of motions cause more reduction in the effective stresses in the surrounding sand and the embedded structures become more vulnerable.

The variations of normalized lateral displacements (u/H) under different peak amplitude of base motions are shown in Figs. 11(a) and 11(b) for the dry and the saturated sand, respectively. It is found that in the case of dry sand, for peak amplitudes of 0.1g, 0.15g, and 0.2g, the maximum (normalized) lateral displacements (u/H) are 0.0033, 0.0061, and 0.0096, respectively, in the numerical analyses. The corresponding values are 0.004, 0.0069, and 0.0095 for the peak amplitude of 0.1g, 0.15g, and 0.2g in the laboratory experiments. When the amplitudes of the base motions are increased from 0.1g to 0.15g and 0.15g to 0.2g, the lateral displacements (u/H) of the walls have increased by 85% and 57%, respectively, as per the numerical analyses. The lateral displacement (u/H) of the wall is increasing with the amplitude of the base motions but the rate of increment is decreasing. These results are also showing that for all the cases considered in this study for the dry sand, the maximum lateral displacement of the walls obtained from the experiments and the numerical analyses is less that 1% of the total height of the cantilever of the walls.

In saturated sand, for the peak amplitude of the base motions of 0.1g, 0.15g, and 0.2g, the maximum (normalized) lateral displacements (u/H) are 0.0501, 0.0710 and 0.0836, respectively in the numerical analyses. They are found to be 0.041, 0.069, and 0.1022, respectively in the corresponding laboratory experiments. From the numerical analyses, the lateral displacements (u/H) increase by 42% and 18%, for the increment of the peak base motions from 0.1g to 0.15g and 0.15g to 0.2g, respectively. Thus, similar to the cases for the walls embedded in dry sand, the lateral displacements (u/H) are increasing with the amplitudes of the base motions, but the rate of increment is decreasing. In the cases of the saturated sand, the maximum lateral displacement (u) of the embedded cantilever wall is 10% of the total height of the wall (H) as the peak amplitude of the base motion reaches 0.2g. This value is only 1% in case of walls embedded in dry sand.

The normalized bending moment ($M/\gamma' H^3$) under different amplitude of the base motions is presented in Figs. 12(a) and 12(b) for the dry and the saturated sand, respectively. It may be observed that the maximum bending moment occurs below the excavation level for all the cases. In case of the walls embedded in the saturated sand, the location of the maximum bending moment in the

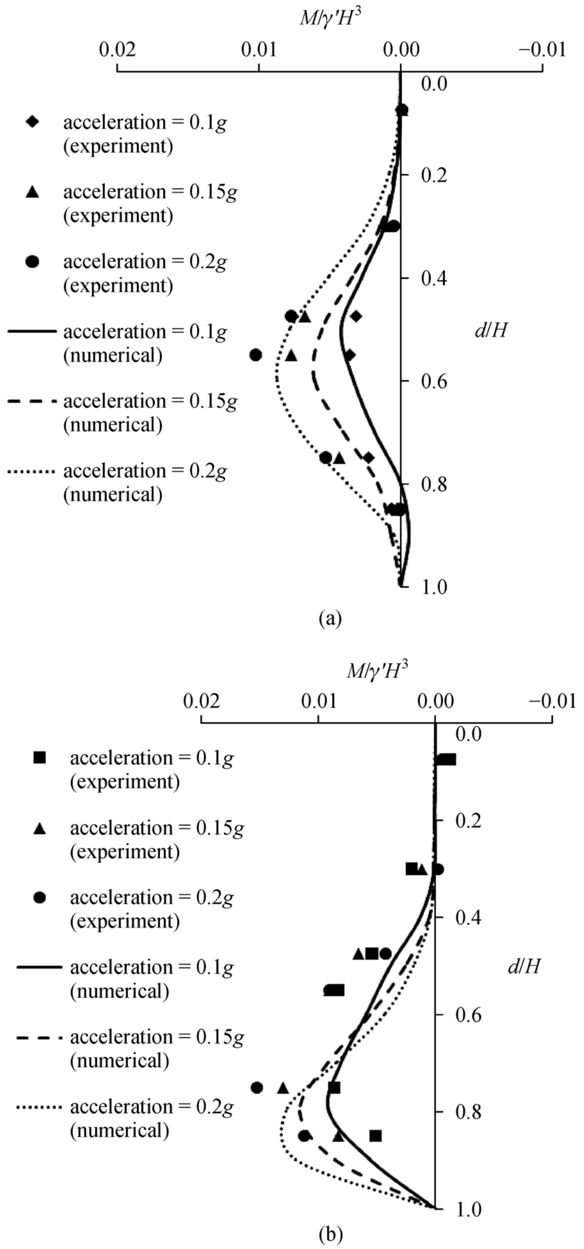

Fig. 12 Bending moments in the embedded cantilever wall under different peak amplitude of base motions in (a) dry soil, (b) saturated soil.

wall shifts downward as compared to it in case of the dry sand. The normalized bending moment ($M/\gamma'H^3$) for 0.1g, 0.15g, and 0.2g peak amplitude of base motions in case of dry sand are 0.0042, 0.0061, and 0.0087, respectively, from the numerical analyses and these values are 0.0036, 0.0077, and 0.0102, respectively, from the experimental study. The maximum bending moment ($M/\gamma'H^3$) has increased by 45% and 43% in the numerical analyses, when the amplitude of the base motions is increased from 0.1g to 0.15g and 0.15g to 0.2g, respectively. In case of saturated sand, the normalized bending moments ($M/\gamma'H^3$) in the embedded walls are 0.0091, 0.0115, and 0.0127 from the numerical analyses and 0.0086, 0.0130, and 0.0152 in the laboratory experiments for 0.1g, 0.15g, and 0.2g base motions, respectively . When the amplitude of the base motions increases from 0.1g to 0.15g and 0.15g to 0.2g, the maximum bending moment ($M/\gamma'H^3$) in the embedded cantilever walls has increased by 26% and 10%, respectively, in the numerical analyses. The maximum bending moment ($M/\gamma'H^3$) in the walls is increasing with the amplitude of the base motions but the rate of increment is decreasing.

It is clearly observed from the above discussions that the peak amplitude of the base motions is an important parameter and it influences the performances of a cantilever wall embedded in both dry and saturated sand. It is also observed from the results that the maximum lateral displacements and the maximum bending moments are increasing with the increment of the peak amplitude of the base motions but the rate of increment is decreasing subsequently.

5.2 Effect of excavation depth (D_e)

The experimental and the numerical analyses are performed on the cantilever walls embedded in dry and saturated sand with different depth of excavation (D_e) between walls. The maximum normalized lateral displacement (u/H) and the normalized bending moment ($M/\gamma'H^3$) along the wall depth, for different excavation depth are obtained from the numerical analyses and the laboratory model tests. The total height of the wall (H) is kept same for all the cases but the excavation depth (D_e) is changed. The amplitude of the base motions is also kept same at 0.1g as shown in Fig. 3(a) for the all these tests (CW1, CW4, CW5, CWU1, CWU4, CWU5). It is found that the value of u/H reduces with the reduction of the excavation depth (D_e/H) in both dry and saturated sand as the embedment depth (D_b) of the wall increases. When embedment depth (D_b) is increased, the passive resistances in the sand are also increasing which help resist the lateral displacements of the wall. It may be seen from Fig. 13 that the value of pore water pressure ratio (r_u) is increasing with D_e/H increasing. When D_e/H is 0.3, the pore water pressure ratio (r_u) is closed to 0.4. But when D_e/H is increased to 0.4 and 0.5, the pore pressure ratio (r_u) in the sand becomes almost 0.6 and 0.7, respectively. For the case of higher D_e/H values, more damages are expected for the walls. The values of the pore water pressure ratios (r_u) have not reached unity for all the cases considered, so complete liquefaction of the sand are not occurring.

The lateral displacements of the right cantilever wall (u/H), at the end of the cyclic loadings for the excavation depths (D_e/H) of 0.3, 0.4, and 0.5, are presented in Figs. 14(a) and 14(b) for the dry and the saturated sand, respectively. In the case of the walls embedded in the dry sand, the maximum lateral displacements of the right cantilever wall (u/H) for the excavation depth (D_e/H) of

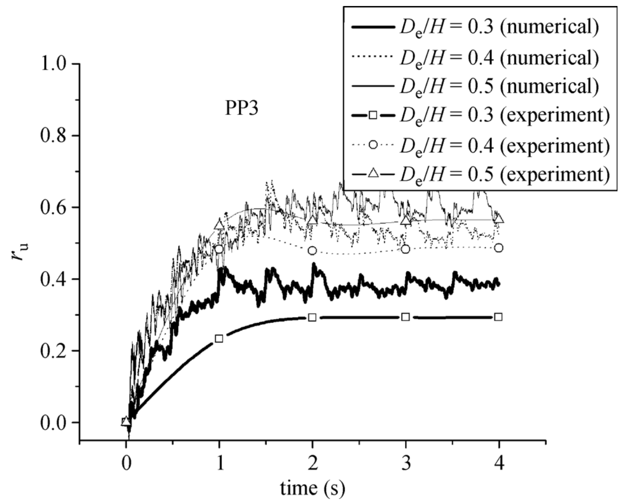

Fig. 13 Variation of pore pressure ratios (r_u) at PP3 with time for different excavation depths (D_e/H).

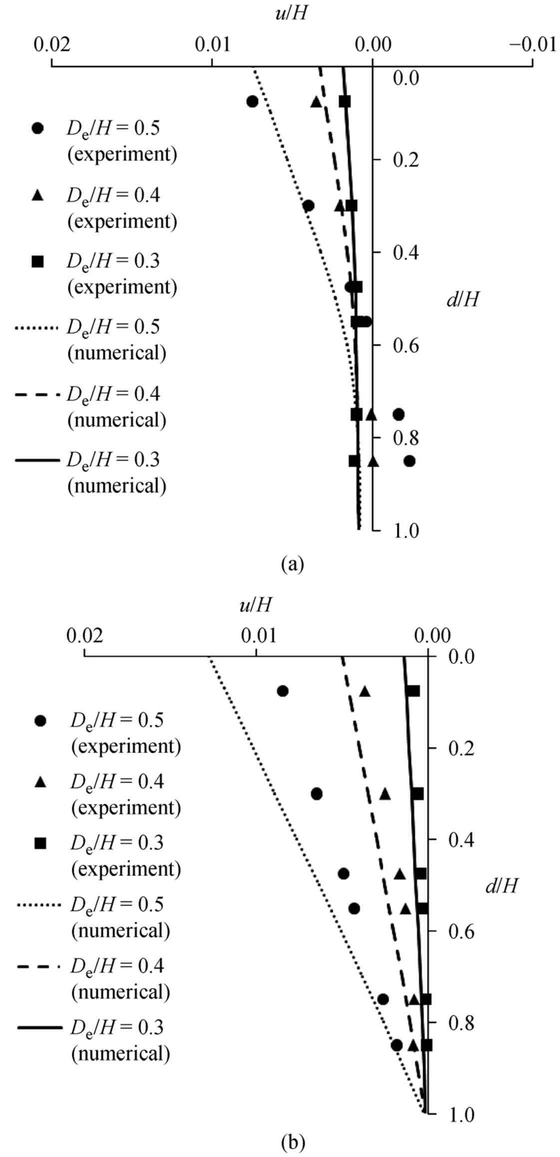

Fig. 14 Lateral displacements of the embedded cantilever wall at different depth of excavation in (a) dry sand and (b) saturated sand.

0.3, 0.4, and 0.5 are found to be 0.0018, 0.0033, and 0.0074, respectively, from the numerical analyses. These values are 0.0019, 0.0040, and 0.0087, respectively, from the corresponding laboratory model tests. The maximum lateral displacement of the embedded cantilever wall is below 1% in dry sand. It is also observed that when D_e/H is reduced from 0.5 to 0.4, u/H gets reduced by 55% in the numerical analyses. But when D_e/H is further reduced from 0.4 to 0.3, the value of u/H reduces by 45%.

In case of cantilever wall embedded in saturated sand, the maximum lateral displacements of the right cantilever wall (u/H), with the excavation depth (D_e/H) of 0.3, 0.4 and 0.5, are found to be 0.014, 0.0501, and 0.1275, respectively, in the numerical analyses and 0.0094, 0.041, and 0.0912, respectively, in the corresponding laboratory experiments. It is observed in the numerical analyses that when D_e/H is reduced from 0.5 to 0.4, u/H reduces by 61%. But when D_e/H is further reduced from 0.4 to 0.3, the value of u/H reduces by 72% in the numerical analyses. Therefore, the rate of reduction in the value of u/H with the reduction of D_e/H is increasing in saturated sand. It is also observed that the maximum lateral displacement of the embedded cantilever wall is below 1% in dry sand but it goes up to 12.75% in saturated sand.

The variations of bending moments ($M/\gamma'H^3$) at different excavation depth (D_e/H) in the dry and the saturated sand are shown in Figs. 15(a) and 15(b), respectively. In case of dry sand, the maximum bending moment in the cantilever wall ($M/\gamma'H^3$) at the excavation depths (D_e/H) of 0.3, 0.4, and 0.5 are found to be 0.0016, 0.0042, and 0.0087, respectively, from the numerical analyses. These values are 0.0024, 0.0036, and 0.0077, respectively, from the corresponding laboratory experiments. When D_e/H is reduced from 0.5 to 0.4, the maximum $M/\gamma'H^3$ reduces by 52%. But when D_e/H is further reduced from 0.4 to 0.3, the maximum $M/\gamma'H^3$ reduces by 62% in the numerical analyses. So, the rate of reduction in the maximum moment in the cantilever embedded wall is increasing with the further reduction in the excavation depth (D_e/H). If there is any restriction of the maximum moment then reduction of depth can be helpful but it will be uneconomic design. Therefore according to the permissible criteria proper depth of excavation can be chosen.

In case of saturated sand, the maximum bending moment in the right cantilever wall ($M/\gamma'H^3$) for the excavation depth (D_e/H) of 0.3, 0.4, and 0.5 are found to be 0.0063, 0.0091, and 0.0178, respectively, in the numerical analyses. The corresponding values are 0.0059, 0.0086, and 0.0151, respectively, from the laboratory experiments.

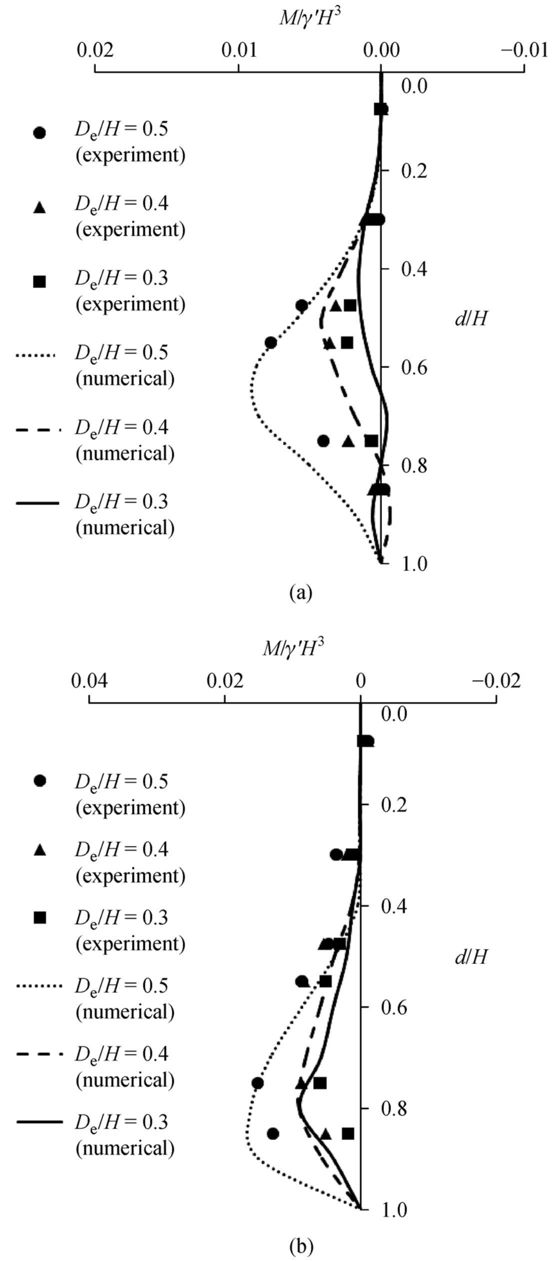

Fig. 15 Bending moments in the embedded cantilever wall with different excavation depths (D_e/H) in (a) dry sand and (b) saturated sand.

In case of walls embedded in saturated sand, when D_e/H is reduced from 0.5 to 0.4, the maximum $M/\gamma'H^3$ reduces by 49%. When D_e/H is further reduced from 0.4 to 0.3, the maximum value of $M/\gamma'H^3$ reduces by 31% in the numerical analyses. The rate of reduction in moments in the walls is decreasing with the further reduction in D_e/H. Thus, one may conclude that the depth of excavation (D_e/H) between the embedded cantilever walls influences the performance of the walls significantly under cyclic loading.

6 Conclusions

The dynamic performances of a pair of cantilever walls embedded in dry and saturated sand and subjected to sinusoidal loadings have been studied using small scale model tests on the shake table and numerically using FLAC2D. The numerical results are found to be in good agreement with the corresponding shake table test results. Based on the results of the present study, the following conclusions can be made.

1) It is observed that the maximum lateral displacement (u) of an embedded cantilever wall occurs at the top of the wall in both, dry and saturated sand, while the maximum bending moment (M) in the wall occurs below the bottom of the excavation.

2) In case of saturated sand, the generation of pore water pressures within the sand is higher under the excavation level as compared to the other places within the sand. This makes the sand below the excavation level weaker in strength.

3) The maximum lateral displacement of the cantilever walls is noticed at the end of the seismic events in both dry and saturated sand. The maximum bending moment in the wall also occurs at the end of the seismic event in the dry sand. But, in the saturated sand, the maximum bending moment in the walls occurs during the motions.

4) From the numerical studies with different excavation depths, it is found that when the depth of excavation between the cantilever walls (D_e/H) reduces from 0.5 to 0.4, the maximum (normalized) lateral wall displacement (u/H) reduces by 55% and 61%, while the maximum moment in the walls ($M/\gamma'H^3$) reduces by 52% and 49% in the dry and the saturated sand, respectively. But when (D_e/H) reduces from 0.4 to 0.3, the maximum lateral displacement (u/H) of the walls reduces by 45% and 72%, and the maximum moment, $M/\gamma'H^3$, in the walls reduces by 62% and 31% in the dry and the saturated sand, respectively. So the depth of excavation plays an important role on the performance of an excavation supported by flexible cantilever walls.

5) The maximum lateral displacement of the embedded cantilever walls due to dynamic loadings is below 1% of the wall height in the dry sand. But, due to the influences of pore water pressure generation within saturated sand during the dynamic loadings, the maximum lateral displacement of the walls can go up to 12.75%.

Acknowledgements The funding for this study vide Grant No. SR/S3/MERC-0029/2011 of SERB, Department of Science and Technology, New Delhi (India) is gratefully acknowledged.

References

1. Boscardin M D, Cording E J. Building response to excavation-induced settlement. Journal of the Geotechnical Engineering

Division, ASCE, 1989, 115(1): 1–21

2. Zahmatkesh A, Choobbasti A J. Evaluation of wall deflections and ground surface settlements in deep excavations. Arabian Journal of Geosciences, 2015, 8(5): 3055–3063
3. Rabczuk T, Zi G, Bordas S, Nguyen-Xuan H. A simple and robust three-dimensional cracking-particle method without enrichment. Computer Methods in Applied Mechanics and Engineering, 2010, 199(37–40): 2437–2455
4. Rabczuk T, Belytschko T. Cracking particles: A simplified meshfree method for arbitrary evolving cracks. International Journal for Numerical Methods in Engineering, 2004, 61(13): 2316–2343
5. Ren H, Zhuang X, Cai Y, Rabczuk T. Dual-horizon peridynamics. International Journal for Numerical Methods in Engineering, 2016, 108(12): 1451–1476
6. Ren H, Zhuang X, Rabczuk T. Dual-horizon peridynamics: A stable solution to varying horizons. Computer Methods in Applied Mechanics and Engineering, 2017, 318: 762–782
7. Areias P, Reinoso J, Camanho P P, César de Sá J, Rabczuk T. Effective 2D and 3D crack propagation with local mesh refinement and the screened Poisson equation. Engineering Fracture Mechanics, 2018, 189: 339–360
8. Zhou S W, Xia C C. Propagation and coalescence of quasi-static cracks in Brazilian disks: An insight from a phase field model. Acta Geotechnica, 2018, 14: 1–20
9. Zhou S, Rabczuk T, Zhuang X. Phase field modeling of quasi-static and dynamic crack propagation: COMSOL implementation and case studies. Advances in Engineering Software, 2018, 122: 31–49
10. Zhou S, Zhuang X, Rabczuk T. A phase-field modeling approach of fracture propagation in poroelastic media. Engineering Geology, 2018, 240: 189–203
11. Zhou S, Zhuang X, Zhu H, Rabczuk T. Phase field modelling of crack propagation, branching and coalescence in rocks. Theoretical and Applied Fracture Mechanics, 2018, 96: 174–192
12. Zhou S, Zhuang X, Rabczuk T. Phase-field modeling of fluid-driven dynamic cracking in porous media. Computer Methods in Applied Mechanics and Engineering, 2019, 350(15): 169–198
13. Okabe S. General theory of earth pressures. Journal of the Japan Society of Civil Engineering, 1926, 12(1): 311
14. Mononobe N, Matsuo H. On the determination of earth pressure during earthquakes. In: Proceedings of the World Engineering Congress. Tokyo, 1929, 9:177– 185
15. Steedman R S, Zeng X. The influence of phase on the calculation of pseudo-static earth pressure on a retaining wall. Geotechnique, 1990, 40(1): 103–112
16. Richards R J, Elms D. Seismic behavior of gravity retaining wall. Journal of the Geotechnical Engineering Division, ASCE, 1979, 150(4): 449–464.
17. Callisto L, Soccodato F M. Seismic design of flexible cantilever retaining walls. Journal of Geotechnical and Geoenvironmental Engineering, ASCE, 2010, 136(2): 344–354
18. Conti R, Viggiani G M B, Burali D'Arezzo F. Some remarks on the seismic behaviour of embedded cantilevered retaining walls. Geotechnique, 2014, 64(1): 40–50
19. Khosrojerdi M, Pak A. Numerical investigation on the behavior of the gravity waterfront structures under earthquake loading. Ocean Engineering, 2015, 106: 152–160
20. Tricarico M, Madabhushi G S P, Aversa S. Centrifuge modeling of flexible retaining walls subjected to dynamic loading. Soil Dynamics and Earthquake Engineering, 2016, 88: 297–306
21. Chowdhury S S, Deb K, Sengupta A. Behavior of underground strutted retaining structure under seismic condition. Earthquakes and Structures, 2015, 8(5): 1147–1170
22. Flogeras A K, Papagiannopoulos G A. On the seismic response of steel buckling-restrained braced structures including sand-structure interaction. Earthquakes and Structures, 2017, 12(4): 469–478
23. Wood J H. Earthquake induced sand pressure on structure. Dissertation for the Doctoral Degree. Pasadena: California Institute of Technology, 1973, 73–05
24. Nadim F, Whitman R V. Seismic induced movement of retaining walls. Journal of the Geotechnical Engineering Division, ASCE, 1983, 109(7): 915–931
25. Finn W D L, Yogendrakumar M, Otsu H, Seedman R S. Seismic response of a cantilever retaining wall: Centrifuge model test and dynamic analysis. In: Proceedings of the 4th International Conference on Soil Dynamics & Earthquake Engineering. Southampton: Computational Mechanics Inc., 1989, 331–431
26. Veletsos A, Younan A H. Dynamic sand pressure on rigid vertical walls. Earthquake Engineering & Structural Dynamics, 1994, 23(3): 275–301
27. Veletsos A S, Younan A H. Dynamic sand pressures on vertical walls. In: Proceedings of the 3rd International Conference on Recent Advance in Geotechnicak Earthquake Engineering & Soil Dynamics. Rolla: University of Missouri, 1995, 1589–1604
28. Veletsos A S, Younan A H. Dynamic response of cantilever retaining walls. Journal of the Geotechnical Engineering Division, ASCE, 1997, 123(2): 161–172
29. Green R A, Olgun C G, Ebeling R M, Cameron W I. Seismically induced lateral earth pressures on a cantilever retaining wall. In: The 6th US Conference & Workshop on Lifeline Earthquake Engineering (TCLEE2003). Long Beach, CA: American Society of Civil Engineers, 2003
30. Ostadan F. Seismic sand pressure for building walls: An updated approach. Soil Dynamics and Earthquake Engineering, 2005, 25(7–10): 785–793
31. Madabhushi S P G, Zeng X. Seismic response of flexible cantilever retaining wall with dry backfill. Geomechanics & Geoengineering, 2006, 1(4): 275–289
32. Madabhushi S P G, Zeng X. Simulating seismic response of cantilever retaining walls. Journal of the Geotechnical Engineering, 2007, 133(5): 539–549.
33. Lombardi D, Bhattacharya S, Scarpa F, Bianchi M. Dynamic response of a geotechnical rigid model container with absorbing boundaries. Soil Dynamics and Earthquake Engineering, 2015, 69: 46–56
34. Meymand P J. Shaking table scale model tests of nonlinear sand-pile-superstructure interaction in soft clay. Dissertation for the Doctoral Degree. Berkeley: University of California, Berkeley, 1998
35. Seed H B, Idriss I M. Simplified procedure for evaluating sand liquefaction potential. Journal of the Soil Mechanics and Foundations Division, 1971, 97(9): 1249–1274
36. Banerjee R, Konai S, Sengupta A, Deb K. Shake table tests and numerical modeling of liquefaction of Kasai River sand. Geotech-

nical and Geological Engineering, 2017, 35(4): 1327–1340
37. Tsuchida H. Prediction and counter measure against the liquefaction in sand deposits. In: Proceedings of the Seminar of the Port and Harbour Research Institute. Yokosuka: Ministry of Transport, Japan, 1970
38. Itasca. FLAC Fast Lagrangian Analysis of Continua, V. 5.0, User's Manual. 2005
39. Callisto L, Soccodato F A, Conti R. Analysis of the seismic behaviour of propped retaining structures. In: Geotechnical Earthquake Engineering and Soil Dynamics IV Conference. Sacramento, California: Geo-Institute of the ASCE, 2008
40. Callisto L, Soccodato F M. Seismic analysis of an embedded retaining structure in coarse-grained sands. In: Proceedings of the 4th International Conference on Earthquake Gotechnical Engineering. Thessaloniki: Springer, 2007
41. Callisto L, Soccodato F M. Performance-based design of embedded retaining walls subjected to seismic loading. In: Proceedings and Workshop: Eurocode 2009. Brussels: The European Committee for Standardization, 2009
42. Callisto L. Capacity design of embedded retaining structures. Geotechnique, 2014, 64(3): 204–214
43. Janbu N. Soil compressibility as determined by Oedometer and Triaxial Tests. In: European Conference on Soil Mechanics & Foundation Engineering. Wiesbaden: Deutsche Gesellschaft für Erd-und Grundbau e.V., 1963
44. Chattaraj R, Sengupta A. Liquefaction potential and strain dependent dynamic properties of Kasai River sand. Soil Dynamics and Earthquake Engineering, 2016, 90: 467–475
45. Hardin B O, Drnevich V P. Shear modulus and damping in sands. Journal of the Soil Mechanics and Foundations Division, 1972, 98(7): 667–692
46. Aggour M S, Zhang J X. Degradation of sands due to combined sinusoidal loading. Journal of Geotechnical and Geoenvironmental Engineering, 2006, 132(12): 1628–1632
47. Ishibashi I, Zhang X. Unified dynamic shear moduli and damping ratios of sand and clay. Soil and Foundation, 1993, 33(1): 182–191
48. Kramer S L. Geotechnical Earthquake Engineering. New Delhi: Pearson Education, 1996
49. Martin G R, Finn W D L, Seed H B. Fundamentals of liquefaction under cyclic loading. Journal of the Geotechnical Engineering Division, ASCE, 1975, 101(5): 423–438
50. Byrne P. A cyclic shear-volume coupling and pore-pressure model for sand. In: Proceedings of the Second International Conference on Recent Advances in Geotechnical Earthquake Engineering and Soil Dynamics. St. Louis, Missouri: University of Missouri-Rolla, 1991, 47–55